ADVANCED MATERIALS
www.advmat.de

# Anisotropic Morphing in Bistable Kirigami through Symmetry Breaking and Geometric Frustration

*Chuan Qiao, Filippo Agnelli, Deepak Kumar Pokkalla, Nicholas D'Ambrosio, and Damiano Pasini**

**Shape morphing in bistable kirigami enables remarkable functionalities appealing to a diverse range of applications across the spectrum of length scale. At the core of their shape shifting lies the architecture of their repeating unit, where highly deformable slits and quasi-rigid rotating units often exhibit multiple symmetries that confer isotropic deployment obeying uniform scaling transformation. In this work, symmetry breaking in bistable kirigami is investigated to access geometric frustration and anisotropic morphing, enabling arbitrarily scaled deployment in planar and spatial bistable domains. With an analysis on their symmetry properties complemented by a systematic investigation integrating semi-analytical derivations, numerical simulations, and experiments on elastic kirigami sheets, this work unveils the fundamental relations between slit symmetry, geometric frustration, and anisotropic bistable deployment. Furthermore, asymmetric kirigami units are leveraged in planar and flat-to-3D demonstrations to showcase the pivotal role of shear deformation in achieving target shapes and functions so far unattainable with uniformly stretchable kirigami. The insights provided in this work unveil the role of slit symmetry breaking in controlling the anisotropic bistable deployment of soft kirigami metamaterials, enriching the range of achievable functionalities for applications spanning deployable space structures, wearable technologies, and soft machines.**

## 1. Introduction

Perforating a thin sheet with a distinct motif of slits has been leveraged in kirigami metamaterials to attain auxeticity, shape shifting, multistable deployment, and other unusual responses.[1–13] In contrast to other shape-morphing metamaterials, such as folded tessellations (origami)[14–16] and bilayer films,[17,18] kirigami patterns can easily achieve fairly complex in-plane and out-of-plane deformations through the opening of rationally designed cuts, making them appealing in a range of sectors, from aerospace deployable structures,[19,20] solar cells,[21] biomedical devices,[22,23] and robotics.[24–27]

The diverse set of properties and functionality that a planar kirigami pattern can deliver stems mainly from the tessellation of its repeating shape, e.g., triangular (kagome pattern), square, hexagonal, and other polygonal tiles, each embedding an intrinsic symmetry of their constituent slits, e.g., rotational, reflectional, and glide reflectional symmetry.[28–33] While ordinary kirigami patterns have been extensively studied for both their linear and nonlinear responses, other less trivial motifs of threefold and fourfold rotational symmetry have attracted attention for being able to offer bistable auxetic deployment with reconfiguration into states of preserving shape.[3] Other studies have focused on more complex incision patterns, e.g., hierarchical[1,34] and fractal tilings,[35,36] with reduced order of symmetry as well as beyond periodicity, e.g., randomly oriented[4] and other aperiodic patterns,[37,38] all contributing to yield a plethora of kinematic and mechanical responses. Approaches leveraging inverse design formulations have also been explored with the aim of programming morphing on target and conformal mapping to predefined surfaces of nearly arbitrary Gaussian curvatures.[5,6,10,39,40] All these investigations confirm the key role that slit symmetry plays in the kinematics and mechanics of kirigami tessellations, a notion that goes well beyond kirigami and applies across the spectrum of solids, e.g., crystals and other architected materials.[41]

Symmetry has long been a valuable tool for creating complex architected materials.[41–44] However, for kirigami metamaterials it has only been applied to rigid deployable patterns[28,29,45] with kinematics described by nondeformable panels and pure rotational hinges. The deployment of all these patterns does not involve geometric frustration,[46,47] a phenomenon occurring when incompatible geometric constraints impede the

C. Qiao
MOE Key Laboratory of Deep Earth Science and Engineering
College of Architecture and Environment
Sichuan University
Chengdu 610065, China

C. Qiao, F. Agnelli, D. K. Pokkalla, N. D'Ambrosio, D. Pasini
Department of Mechanical Engineering
McGill University
Montréal, Québec H3A 0C3, Canada
E-mail: damiano.pasini@mcgill.ca

The ORCID identification number(s) for the author(s) of this article can be found under https://doi.org/10.1002/adma.202313198



**DOI: 10.1002/adma.202313198**

deformation of an object under a set of applied forces; in the realm of kirigami, geometric frustration appears as local disordered deployments caused by incompatible geometric restrictions, such as local deformation of panels due to slit geometry that violates rigid deployable constraints[48] and out-of-plane morphing due to nonuniform strains in nonperiodic patterns.[37] This focus has so far excluded the investigation of exotic modes of deformation, e.g., anisotropic and inhomogeneous deployment,[49] pattern formation of complex order,[47] and history-dependent mechanical computation[50] among other functionalities, that—on the other hand—have been studied in frustrated soft metamaterials. The concept of geometric frustration in soft kirigami and its interplay with slit symmetry remains elusive and calls for further investigation due to its promise to unlock shape transformations and properties thus far unattainable in kirigami metamaterials.

With a focus on soft kirigami metamaterials, this work aims to unveil the intrinsic relation between slit symmetry, geometric frustration, and anisotropic scaling in a representative class of uniformly scaled bistable auxetic kirigami. By breaking slit symmetry and allowing sheet deformability, we demonstrate how to program their anisotropic bistable deployment, departing from uniform scaling transformations that are frustration-free to nonuniform scaling transformations that are geometrically frustrated. Through a combined approach of semi-analytical derivations, numerical simulations, and experiments, we map the symmetry relations of bistable kirigami and investigate their role on bistability, anisotropy, deployment magnitude as well as geometrically frustrated deployed state. We showcase the insights gained from our investigation through two demonstrations. The first demonstrates a set of anisotropic in-plane deployments of bistable kirigami that leverage shearing deformations to achieve target shapes and functions. The second employs a simple yet comprehensive shape target that simultaneously contains positive, negative, and zero Gaussian curvatures to show the potential of arbitrarily scaled kirigami for generic flat-to-3D deployment, hence proposing a design strategy for anisotropic shape-morphing of kirigami sheets.

## 2. Results

### 2.1. Geometry Description, Symmetry Relations, and Scaling Transformation of Unit Cell

We focus on a representative class of kirigami, bistable auxetic metamaterials (BAM),[3] that are frustration-free in their stable states (initial and final) and isotropically deploy through a uniform scaling transformation. Their geometry consists of rotating equilateral triangles that are surrounded by translational Y-strut motifs, which are periodically tessellated with threefold rotational symmetry. In BAM, geometric frustration is encountered only in state transition, i.e., during deployment, where the rotating units uniformly push away their neighboring translational Y-strut motifs in all directions and impart isotropic scaling to their deployment.

To study the interplay between slit symmetry and geometric frustration, we now focus on an arbitrary kirigami unit (**Figure 1A**) where we break the threefold symmetry of their slits. Our goal is to investigate the physical mechanisms underpinning nonuniform deployment and its frustrated equilibrium states, the signature of anisotropic bistable auxetic metamaterials (ABAM). The periodic pattern of ABAM consists of six mutually intersecting slits nesting two triangle units each within a larger triangular module. To describe ABAM in a compact and insightful form, we focus on a subset of geometric parameters, i.e., the internal angles $\varphi_1$, $\varphi_2$, and $\varphi_3$, that govern the symmetry of the kirigami pattern, and present a ternary plot where the internal angles lie on its axes (Figure 1B). Each point in the parameter space is defined by a set of $\varphi_i$ ($i$ = 1, 2, and 3) values (gray isoangle lines) that can describe the geometry of any slit pattern applied to a unit cell with prescribed base length $\ell_1$, internal cut ratio $a_1/\ell_1$, and normalized hinge thickness $t/\ell_1$. For example, the intersection (red dot) of the three bisectors ($\varphi_1 = \varphi_2 = \varphi_3$) denotes a kirigami pattern with an equilateral elementary triangle that belongs to the "p31m" wallpaper group,[28] i.e., its geometry in its two stable states features threefold rotational symmetry and reflectional symmetry. As described above, this is BAM exhibiting geometrical frustration at the intermediate states of deployment whereas its closed and deployed states are frustration-free. By altering the geometry of the elementary triangle, ABAM can access other wallpaper groups with reduced symmetry. For example, if the elementary triangle is isosceles ($\varphi_1 = \varphi_2$, $\varphi_2 = \varphi_3$, or $\varphi_1 = \varphi_3$), ABAM that lie along any of the bisectors of the ternary plot belong to the "cm" class, i.e., there exist reflections and glide reflections with parallel axes. Figure 1B shows two types of "cm" ABAM, one describing a triangle with two long sides and one short side (pattern drawn in blue and ternary plot bisectors with solid lines), or the other with two equal sides shorter than the third side (pattern drawn in orange and ternary plot bisectors with dashed lines). Lastly, the most general case is for ABAM belonging to the "p1" class ($\varphi_1 \neq \varphi_2 \neq \varphi_3$), represented by any point that is not on the bisectors, e.g., green pattern, where there exists neither rotational nor reflectional symmetry.

While the location in the ternary plot determines the symmetry group of ABAM, the symmetry the ternary plot itself conveys important insights on the existence of dissimilar sets of geometric parameters that describe the same ABAM. With the shape of an equilateral triangle, the ternary plot naturally exhibits threefold rotational symmetry around its center and reflection symmetry with respect to its three bisectors. If we take an arbitrary ABAM and denote it as $\mathcal{B}(\varphi_1, \varphi_2, \varphi_3)$, symmetry operations applied to the ternary plot enable to obtain at most six distinct ABAM patterns that are all obtained by the six possible permutations of the angles (e.g., $\mathcal{B}(\varphi_1, \varphi_3, \varphi_2)$ and $\mathcal{B}(\varphi_3, \varphi_1, \varphi_2)$). Since all these six ABAM patterns can be simply obtained through rotational and reflectional operations applied to one of them (Section S7 and Figure S9, Supporting Information), this notion proves that the symmetry of the ternary plot, i.e., the geometric parameter space, correlates with that of their ABAM patterns, the physical space, and that these kirigami patterns are all identical. As a result, the study of the entire parametric space of our ternary plot can be reduced to the model of one of its subsets, e.g., one describing shapes with angles $\varphi_1 < \varphi_2 < \varphi_3$ (or equivalently $\ell_1 < \ell_2 < \ell_3$), i.e., the lower-right region bounded by the red triangle.

Following Neumann's principle,[51,52] the symmetry of physical properties in a crystal can only be higher or equal to the symmetry of the crystal lattice. To enable nonuniform scaling

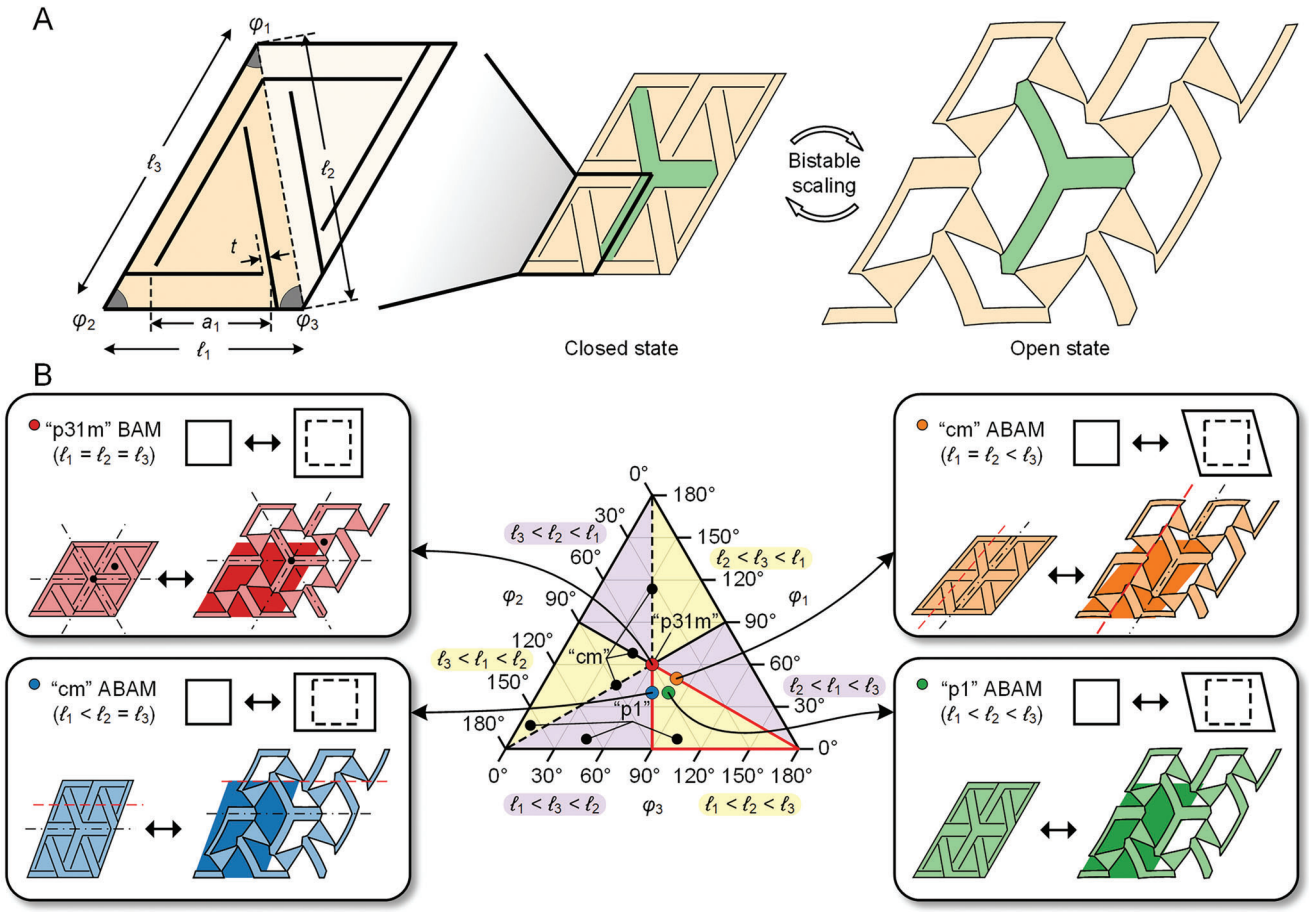


**Figure 1.** Anisotropic Bistable Auxetic Metamaterials (ABAM). A) Triangular building block and corresponding 2 × 2 unit cells in closed state and open state of preserving shape. Y-strut (green) featuring residual bending deformation for generic ABAM. B) Design space visualized in a ternary plot obtained by varying symmetry leading to programmable anisotropic expansion. Four demonstrative cases of ABAM with distinct wallpaper groups illustrate their closed and open states, with symmetry properties highlighted by reflection axes (black dash-dot lines), glide reflection axes (red dashed lines), and rotational centers (black dots). Effective deformations of ABAM are shown in the upper-right corner of each panel.

of deployment, we should thus reduce the symmetry of our uniformly scalable baseline, i.e., BAM. To assess the scaling mode, we now analyze unit cells in their deployed state under periodic boundary conditions while ignoring finite size effects.[3,53] For the "p31m" BAM, we observe that the deployed unit cell also belongs to "p31m" class, and the pertinent strain tensor values must remain unchanged from rotational symmetry operations of angles 120° and −120°. This in turn constrains the strain tensor in the deployed state to carry an isotropic symmetry, i.e., it only permits a uniform change of the scaling factor; here, the internal cut parameters are uniformly scaled during deployment. In ABAM, the unit cells with a lower order of symmetry undergo anisotropic scaling in the deployed state, and cause residual geometric frustration in the Y-strut beams in the open stable state (see the green set of beams in Figure 1A obtained from finite element simulations), whereas the inner triangles appear almost undeformed because the frustration is mitigated by the compliance of slender Y-strut units (Section S2.1, Supporting Information). For "cm" ABAM (Figure 1B), the two beams of equal length exhibit deflections in opposite directions, while the last beam is undeformed, a phenomenon that preserves the "cm" class in the deployed stable state. On the other hand, in "p1" ABAM, all beams of the Y-strut unit are deformed, and the deployed unit cell can exhibit only "p1" symmetry.

### 2.2. Bistability, Anisotropy, and Nonuniform Scaling

To investigate the role of anisotropic scaling during ABAM deployment, we track the evolution of three quantitative measures, each being expressed as a function of the geometrical parameters $\varphi_2$, $\varphi_3$, $a_1/\ell_1$, and $t/\ell_1$:

- Bistability, described by the valley over the peak ratio of the strain energy density $E_{\min}/E_{\max}$
- Anisotropy, measured by the maximum value of engineering shear strain $\gamma_{\max}$ for all choices of direction $\alpha$ in plane, which is obtained from the right Cauchy–Green deformation tensor $C_{ij}$ following finite strain theory:[54]

$$\gamma_{\max} = \max_{\alpha\in[0,2\pi]}\left(\frac{\pi}{2} - \cos^{-1}\frac{C_{12}(\alpha)}{\sqrt{C_{11}(\alpha)\,C_{22}(\alpha)}}\right) \quad (1)$$

- Magnitude of scaling, defined here by the engineering volumetric strain $\varepsilon_V$, computed from the principal in-plane strains $\varepsilon_1$ and $\varepsilon_2$,

$$\varepsilon_V = (1+\varepsilon_1)\ (1+\varepsilon_2) - 1 \tag{2}$$

These strain measures are here selected for simplicity. While other strain measures, such as true strain, could be considered, they would not affect the overall findings in this work.

All the metrics above are obtained through a set of numerical simulations of various unit cells under periodic boundary conditions (Section S5, Supporting Information). The unit cell is initially loaded under uniaxial tension along the horizontal direction beyond its bistable state, and then is released to return the bistable state. Moreover, the deployed state of any generic ABAM can be determined with a good level of accuracy through a semi-analytical model that assumes rigid triangles, Euler–Bernoulli beams, and pure rotational hinges. In our model described in Section S2 (Supporting Information), the open state should satisfy the balance of in-plane bending moments at the junction of three beams without any external work. This translates to:

$$\sum_{i=1,3} \frac{w_i^3}{\lambda_i^2} u_t^{(i)} = 0 \tag{3}$$

where $w_i$ is the width of the $i$-th beam, $\lambda_i$ is the length of the $i$-th beam, expressed as a function of $\varphi_1$, $\varphi_2$, and $\varphi_3$ and $u_t^{(i)}$ are the unknown transverse displacement at the tip of the $i$-th beam. The geometrical constraints imposed by the rigid blocks combined with the periodicity of the pattern provide the two additional equations required to determine $u_t^{(i)}$ that ultimately enable us to describe the ABAM configuration in the deployed state.

**Figure 2A** shows an ABAM unit cell with "cm" symmetry ($\varphi_1 = 40°$, $\varphi_2 = \varphi_3 = 70°$) in its equilibrium states, which are obtained both from our semi-analytical model and numerical simulations with periodic boundary conditions. This unit cell design is representative of the designs shown in Figure 1B. The results are overall in good agreement, although the former does not account for the stretching and compression in the living hinges, hence slightly overestimating the strain level (both normal and shear strains) as shown in the polar plot of Figure 2B. Here, we observe the hourglass-shaped curve of the engineering normal strain $\varepsilon$, indicating the highly anisotropic scaling of the deployed unit cell with a horizontal expansion 200% above its vertical counterpart. The engineering shear strain $\gamma$, which describes the distortion of the material through the measurement of the local changes of angles, is also depicted in the polar plot to quantify the magnitude of the anisotropic distortion of the deployed unit cell along all directions. $\gamma_{max} = 0.38$ is the maximum value that appears at the direction of 45°. Figure 2C shows the evolution of the stress and strain energy density as a function of an effective engineering strain applied to the periodic unit cell along the horizontal directions. The stress curve exhibits a negative stiffness, i.e., the negative slope in the stress-strain plot, around $\varepsilon = 0.5$, until the stress finally transits from negative to positive values. The existence of negative stress leads to a local minimum of the energy density curve $E_{min}$ that is far from the initially undeformed state, where ABAM reach its bistable deployed state. Additionally, we note that ABAM in the bistable state can maintain its shape without external forces (Figure 2C).

Next, we perform a parametric analysis with numerical simulations to unveil the relation between slit symmetry breaking and anisotropic bistable scaling. To manipulate the symmetry properties of ABAM, we sweep the internal angles $\varphi_1$, $\varphi_2$, and $\varphi_3$ between 10° and 160° with an increment of 5°. We first investigate the global parameters by prescribing the hinge thickness ($t/\ell_1 = 0.04$) and the size of the internal triangle ($a_1/\ell_1 = 0.6$) values that ensure bistability for a sizeable range of ABAM patterns. In a second step, we also explore the role of the internal parameters, i.e., the internal triangle size $a_1/\ell_1$ varying from 0.4 to 0.8, to capture the influence of slit symmetry breaking in a broader design space. Although in this work we focus on the role of slit symmetry breaking in elastomer kirigami metamaterials, the choice of other material types could also affect their mechanical response.[55,56]

Figure 2D shows the first set of results of the parametric study, where the bistability index $E_{min}/E_{max}$ is plotted on the ternary plot. What we observe here is the role of symmetry breaking in ABAM, indicating that a departure from symmetry, with the central point being the BAM that has the highest degree of symmetry (p31m), diminishes the energy barrier. The map shows that excessive distortion in the slit pattern hinders bistability and can eventually downgrade ABAM to a monostable kirigami for internal angles $\varphi_i$ ($i = 1$, 2, and 3) above 105°. While ABAM lying on the dashed bisectors (thickset "cm" ABAM) of the ternary plot mark the direction where bistability weakens most rapidly, the maximum engineering shear strain $\gamma_{max}$, i.e., anisotropy (Figure 2E), and the volumetric strain $\varepsilon_V$, i.e., magnitude of scaling (Figure 2F) measured, also show strong dependency on the symmetry group. The slender "cm" ABAM, marked by solid bisectors (e.g., blue pattern in Figure 1B), exhibit the highest levels of anisotropy and normal expansion with large values of shear and volumetric strains, whereas the thickset "cm" ABAM, marked by dashed bisectors (e.g., orange pattern in Figure 1B), tend to exhibit low values of anisotropy and normal expansion. On the other hand, an ABAM of the "p1" symmetry group shows moderate responses bounded by those of the slender and thickset "cm" ABAM (more detail in Section S2 and Figure S3 in the Supporting Information).

The most regular "p31m" BAM provides the highest bistability, while "p1" and "cm" ABAM exhibit a reduced value, but they offer a sizeable tunability for anisotropic scaling. This observation suggests that slit symmetry breaking controls the trade-off between bistability and anisotropy of scaling and Figure 2G shows their antagonistic nature. The "p31m" BAM unit cells with varying size of the inner triangle ($a_1/\ell_1$ from 0.4 to 0.8) show no shear strains (red dots) and are unable to attain anisotropic deployment. For "p1" ABAM, domains with various shear strains can be accessed for all values of $a_1/\ell_1$ from 0.4 to 0.8. Lastly, slender "cm" ABAM (solid lines) form the lower bound of the domains of "p1" ABAM in terms of bistability index $E_{min}/E_{max}$, indicating that the slender "cm" ABAM is the most effective in achieving anisotropic deployment while preserving bistability. In contrast, the thickset "cm" ABAM (dashed lines) is the least bistable among ABAM for a given shear strain.

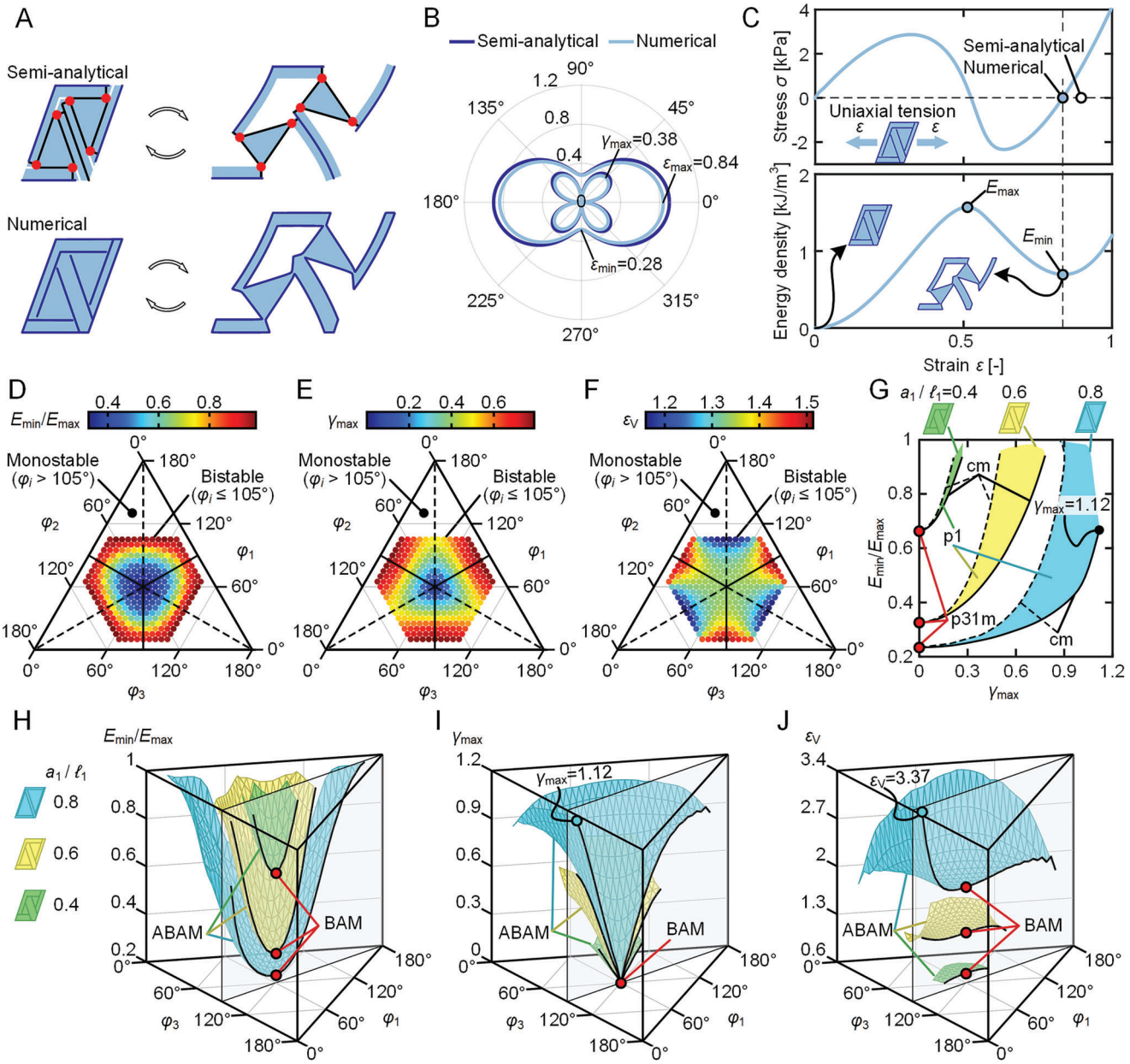


**Figure 2.** Anisotropic mechanical response of ABAM unit cells. A) Cut pattern of representative unit cell ($\varphi_1 = 40°$, $\varphi_2 = \varphi_3 = 70°$) with its deployed state predicted by a semi-analytical model (Section S2, Supporting Information) and numerical simulation. B) Polar plot of engineering normal strain $\varepsilon$ and shear strain $\gamma$ of unit cell. C) Evolution of stress and energy density as a function of strain obtained by numerical simulation under periodic boundary conditions. D–F) Contour plots characterizing energy (bistability $E_{min}/E_{max}$), anisotropy (shear strain $\gamma$), and expansion (volumetric strain $\varepsilon_V$) of ABAM for varying geometric parameters ($\varphi_1$, $\varphi_2$, and $\varphi_3$) and given inner triangle size ($a_1/\ell_1 = 0.6$). Blank regions in ternary plot indicate monostable unit cells with angle $\varphi_i > 105°$ ($i$ = 1, 2, and 3). G) Trade-offs between bistability and anisotropy of ABAM. Colored domains correspond to $a_1/\ell_1$ values (inner triangle size) of 0.4, 0.6, and 0.8. H–J) Cut view of 3D surfaces characterizing energy (bistability $E_{min}/E_{max}$), anisotropy (maximum shear strain $\gamma_{max}$), and expansion (volumetric strain $\varepsilon_V$) of bistable auxetics for varying geometric parameters ($\varphi_1$, $\varphi_2$, $\varphi_3$) and given values of $a_1/\ell_1$ ($t/\ell_1$ = 0.04).

Figure 2 H–J further explores the role of slit symmetry breaking in a broader design space of ABAM. In particular "cm" ABAM ($\varphi_1 = \varphi_2$), taken as representative, is characterized by the three metrics ($E_{min}/E_{max}$, $\gamma_{max}$, and $\varepsilon_V$) in a 3D plot for three values of $a_1/\ell_1$, each visualized by a color in its corresponding section view. As can be observed in Figure 2H, the design space of ABAM expands with $a_1/\ell_1$, while the bistability index $E_{min}/E_{max}$ still increases monotonically for ABAM that departs from the most symmetric BAM, "p31m" ($\varphi_1 = \varphi_2 = \varphi_3 = 60°$). Figure 2 I,J shows that both the shear strain and the volumetric strain are higher for larger values of $a_1/\ell_1$, whereas the "cm" ABAM trace the directions in which the strains vary

either most rapidly or slowly. These results further demonstrate that slit symmetry governs the anisotropic bistable deployment. In some kirigami patterns, a unique and extreme case of strain can be achieved by using the slender "cm" ABAM design. This design features a combination of angles and ratios that result in a maximum engineering shear strain of 1.12 and a maximum volumetric strain of 3.37. This showcases the potential of symmetry breaking in kirigami patterns for creating anisotropic shape morphing. The design is shown in Figure S8 (Supporting Information), while the strain values are depicted in Figure 2 H–J.

### 2.3. From Repeating Unit to ABAM Tessellation: Experimental Characterization of Tensile Response

Through a set of experiments and numerical simulations, we now characterize the anisotropic bistable response in ABAM specimens undergoing a cycle of tension (loading) and compression (unloading) (**Figure 3**; Sections S3 and S5, Supporting Information). Four specimens, designed with given geometry and symmetry group, were laser cut from 6.35 mm thick natural rubber sheets and pulled at a strain rate of 10 mm $min^{-1}$ (Videos S1 and S2, Supporting Information). The periodic array for each sample comprises 5 × 5 unit cells.

Figure 3 shows the bistable responses of all fabricated specimens, able to retain their deployed state even without external load. The deformation observed during the tensile test is typical of a mechanism featuring rotational hinges, where the Y-strut motifs in the "cm" and "p1" ABAM specimens are frustrated, hence being deformed unlike those in the "p31m" BAM specimen (Figure 3). During the tension process, all specimens go through various metastable states before they reach the fully open stable state. In the unloading stage, the negative values in the load–displacement curves demonstrate that the specimens can resist the action of the external compression and maintain their fully open shapes until the compressive load overcomes their energy barrier and guides them back to their initial state (Video S2, Supporting Information). Being monolithic with the rest of the structure, neighboring units undergo relative rotation by hinge bending. As a result, geometric frustrations occur with the relative rotation between the triangles and the Y-strut motifs, a phenomenon that in turn results in structural bistability. We also note that unit cells in the corner do not deploy uniformly as the others do in the middle. This phenomenon occurs because their motion is not confined by adjacent unit cells, and can be avoided by pulling the kirigami with distributed loading.[10,55]

An additional observable feature, which is specific to the ABAM, is the programmable anisotropic deformation of its unit cells, enabling the tailoring of both the magnitude and the direction of nonuniform morphing. In contrast to the "p31m" BAM specimen that expands uniformly in all directions and maintains its macroscopic outline in the deployed state, the "cm" and "p1" ABAM specimens display distinct and tunable expansion in response to the vertical pull, showing an envelope that is dissimilar from its initial undeformed state. To better illustrate the anisotropic deformation of ABAM, a square area was initially painted on the surface of the specimens. In the deployed state, the two "cm" ABAM specimens elongate mainly in the pulled direction but with distinct stretch ratios, whereas the "p1" ABAM specimen mainly expands in an oblique direction.

As per the load–displacement curves, all specimens start with a short linear stage, then enter a saw-toothed plateau that alternates between positive and negative values of stiffness, and finally increase monotonically with the displacement. A large hysteresis loop appears between the loading and unloading curves mainly due to the negative stiffness behavior of the unit cells that dissipate energy via snap-through buckling.[57–59] In our experiments, the energy loss may also be partially attributed to the friction between the specimen and the clamps introduced to suppress out-of-plane buckling as well as the material viscoelasticity of rubber.

The results of our experiments are supported by numerical analyses that capture the overall behavior of the specimens. The load–displacement curves show three major peaks under tension and a negative portion during the compression stage, indicating structural bistability. The first two peaks are caused by the snapping of unit cells around the clamps, and the final peak is caused by the opening of the remaining unit cells (Video S2, Supporting Information). The experimental curves in Figure 3 also show minor peaks in addition to the major peaks in the numerical curves. This factor can be attributed to tiny misalignments and manufacturing defects that emerged during the fabrication of our specimens, which mildly affected the local snap-through events. Our numerical model does not account for these defects.

### 2.4. Programming Planar Bistable Deployment: Anisotropic Snapping

After uncovering the physical mechanism underpinning anisotropic bistable scaling of ABAM, we now showcase its potential for programming planar arbitrary deployment. Our first simple deployment target is a "shear band," which we aim to achieve with an initially rectangular-shaped kirigami. To do so, we start by combining "p31m" and "cm" ABAM unit cells in a rectangular domain (**Figure 4A**). In the initial state, 4 × 4 "cm" ABAM unit cells ($\varphi_1 = \varphi_3 = 45°$ and $\varphi_2 = 90°$) are sandwiched between eight layers of "p31m" BAM unit cells ($\varphi_1 = \varphi_2 = \varphi_3 = 60°$). Once deployed, the "p31m" unit cells expand uniformly in all directions with no shearing, whereas the "cm" unit cells exhibit sizeable shear strains that skew the material by about 25.5°. The outcome is the transformation of the initially rectangular sheet into a "shear band" (Video S3, Supporting Information). As a second example, we add complexity to the planar shape target, aiming to deploy a rectangular-shaped kirigami into a letter "M." Figure 4B illustrates the result where the oblique strokes are formed by the shearing of "cm" unit cells and the other strokes consist of isotropic scaling "p31m" unit cells (Video S4, Supporting Information). In these examples, while "p31m" BAM maintains its initial shape with isotropic expansion in the deployed state, ABAM with reduced symmetry undergo anisotropic scaling with considerable shear strains. The collective shearing of the symmetry-broken kirigami units provides the driving force to distort the material from its initial rectangular shape to a more complex target configuration.

ABAM anisotropy can be leveraged to attain functionality that goes beyond the mere attainment of shape morphing. For example, the bistable shearing of ABAM elements along certain

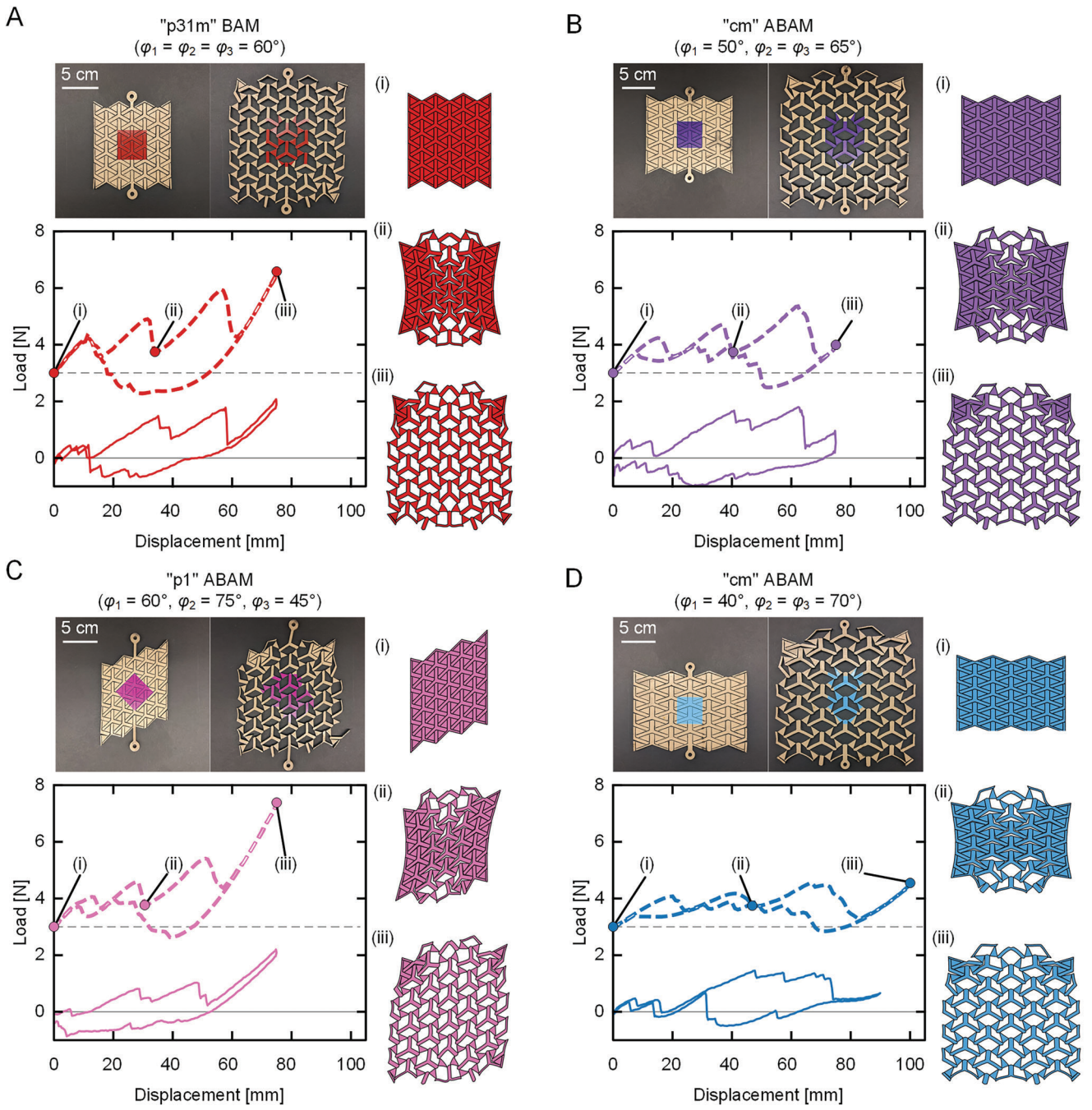


**Figure 3.** A–D) Uniaxial tensile response of BAM and ABAM. Experimental (solid line) and numerical (dashed lines, shifted vertically by 3 N for ease of reading) force–displacement curves during loading (tension) and unloading (compression). $a_1/\ell_1 = 0.6$ and $t/\ell_1 = 0.04$ for all specimens.

preferential directions can be harnessed to enable the transmission of a signal, either mechanical or of another physical nature, between realigned elements. ABAM can thus drive interlocking hooks to realign, engage, and provide resistance to applied tensile forces. Figure 4C shows a demonstrative example where we leverage the shearing of "cm" unit cells ($\varphi_1 = \varphi_3 = 71.6°$, $\varphi_2 = 36.8°$) to control the assembly of a load-bearing mechanism. The "cm" unit cells are initially tessellated in a parallelogram manner, hence enabling them to deploy into a bistable rectangle profile. In this demonstration, the effective shear strain of ABAM is harnessed to align functional components (blue). In the physical realization, a set of acrylic hooks are attached on the surfaces of the translational Y-strut motifs in the "cm" unit cells to act as load-bearing components. When the "cm" unit cells switch to the deployed state, despite being unable to carry heavy load, their realignment makes the hooks to interlock with each other and form a chain that can resist tensile forces (Figure 4D). In Figure 4E, although the ABAM made from 2 mm thick rubber sheet is extremely

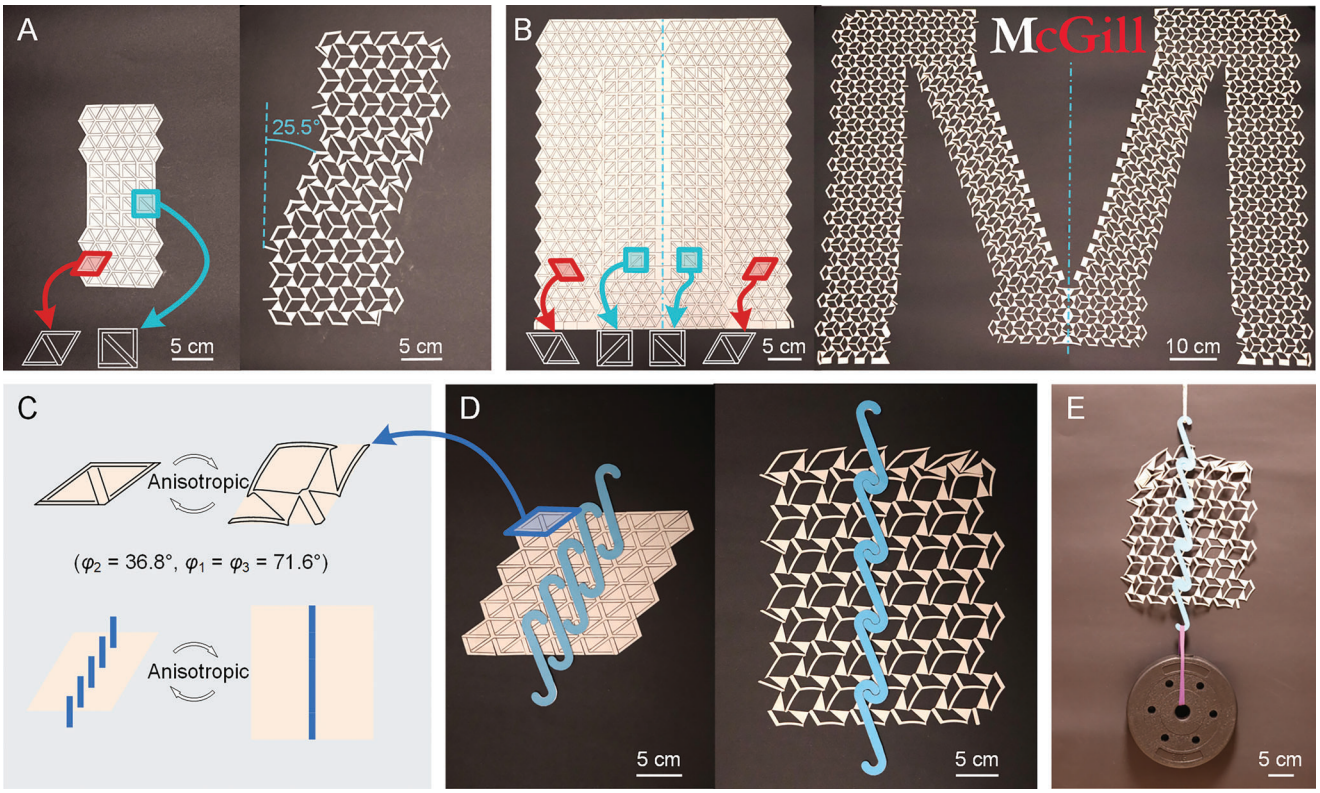


**Figure 4.** Planar deployment of ABAM. A) Shear band composed of "p31m" and "cm" unit cells. B) Letter "M" composed of "p31m" and "cm" unit cells. C–E) Mechanical switch leveraging ABAM shear strain to align rigid hooks (blue) attached to translational Y-strut motifs and delivering load-bearing capacity.

soft and floppy, the augmented ABAM structure can leverage the hooks as an exoskeleton substrate that altogether can withstand a weight of 3 kg (Video S5, Supporting Information). Along with interlock hooks for load-bearing demonstration, ABAM can also be combined with other functional components, such as electrical circuits,[60] imaging devices,[61] and magnetic materials,[62] to achieve a wide range of applications beyond shape morphing.

### 2.5. Programming 3D Bistable Anisotropic Deployment

Besides planar deployment, ABAM can anisotropically deploy from a flat state to a 3D stable shape. To demonstrate this potential, we choose a simple yet comprehensive 3D shape target (**Figure 5A**) that simultaneously contains positive (dome-like surfaces), zero (ruled surfaces), and negative (saddle-like surfaces) Gaussian curvatures. The 3D target comprises three semicylindrical shells, including two perpendicular-cut segments (i) and (iii) at the ends (red), and one oblique-cut segment (ii) in the middle (blue). This shape target ensures that the Gaussian curvature is positive at the peak between segments (i) and (ii), zero within each segment, and negative at the saddle between segments (ii) and (iii).

For simplicity, we assume that the 2D precursors of both the whole 3D target and its constituent segments all have rectangle shapes (Figure 5B). To determine the scaling ratio between the precursor and the target, we first divide the 3D target into three segments (Figure 5C). Segments (i) and (iii) of the target can be flattened as rectangles, but segment (ii), being an oblique-cut semicylindrical shell, can only be flattened as a chevron shape. Comparing the geometry of the flattened targets and their precursors, all segments exhibit changes in their sizes with nonzero volumetric strains $\varepsilon_V \neq 0$. In addition, segment (ii) also displays a nontrivial shear strain $\gamma \neq 0$, which determines the oblique angle $\theta$ of the 3D target (Figure 5G; Section S4, Supporting Information) as:

$$\theta = \cos^{-1}\left(\frac{\pi \cos\gamma - 2}{\pi - 2}\right) \tag{4}$$

To attain isotropic scaling segments (i) and (iii) ($\varepsilon_V \neq 0$ and $\gamma = 0$), we select the "p31m" unit cell ($\varphi_1 = \varphi_2 = \varphi_3 = 60°$), while for the anisotropic scaling segment (ii) ($\varepsilon_V \neq 0$ and $\gamma \neq 0$), we chose a square-shaped "cm" unit cell ($\varphi_1 = \varphi_3 = 45°$, $\varphi_2 = 90°$) to ease the tessellation.

Figure 5D shows the fabricated sample of the 2D precursor, assembled with four columns of "cm" unit cells that are sandwiched between eight columns of "p31m" unit cells. Due to the symmetry of the flattened chevron target, segment (ii) is tessellated with two mirrored packs of 4 × 4 "cm" unit cells. In Figure 5E–G, the deployed state of the sample can tightly match the 3D-printed target surface (Video S6, Supporting Information), which proves the dominant role of shear strain in achieving the target (Equation (4)). This demonstrates the potential of ABAM and

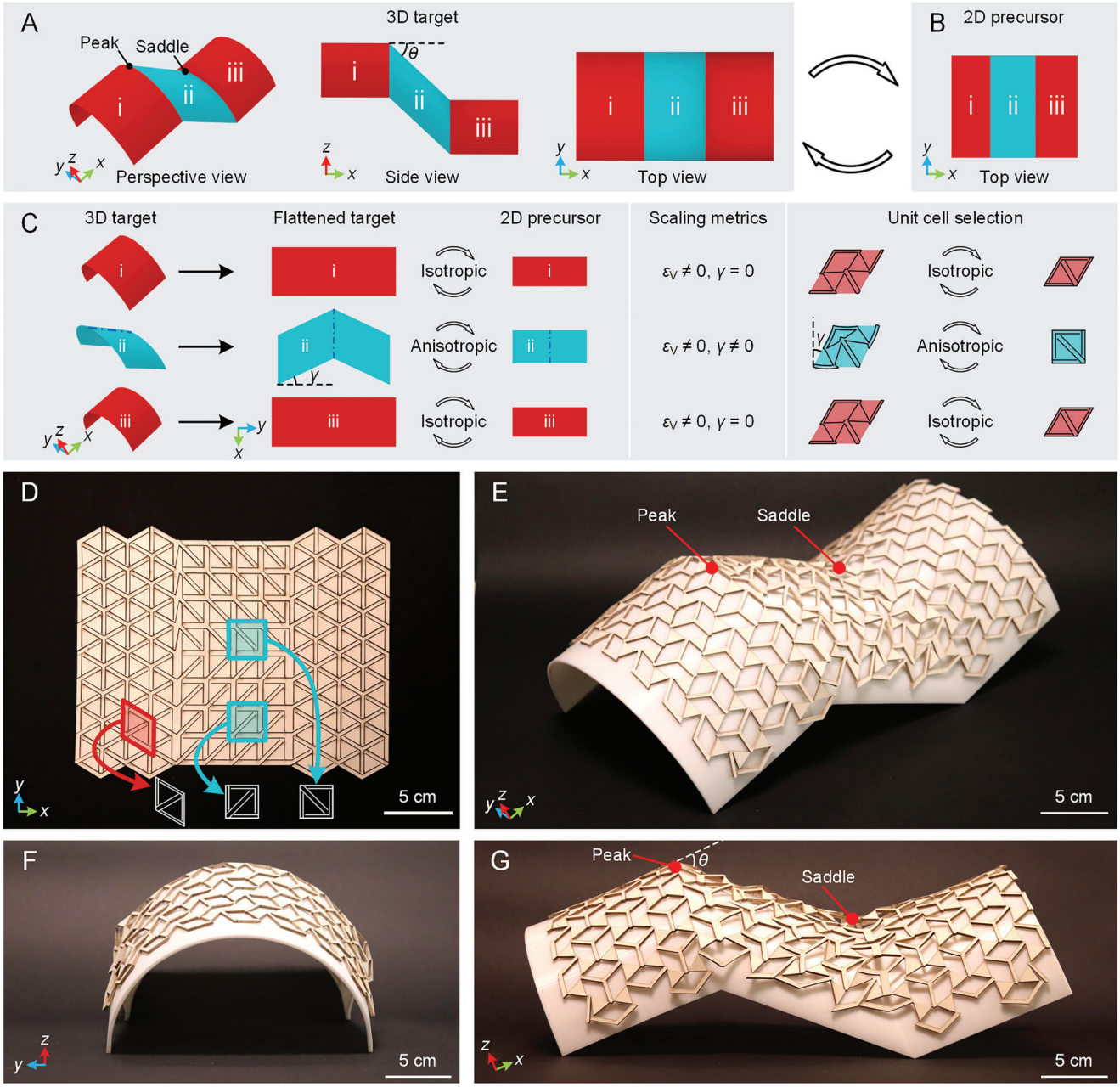


**Figure 5.** 3D bistable deployment of ABAM. A) 3D target shape composed of three semicylindrical shells featuring a peak point and a saddle point. B) 2D precursor of 3D target. C) Unit cell selection. 3D target decomposed into three sections and flattened. Scaling metrics between flattened target and 2D precursor, including volumetric strain $\varepsilon_V$ and shear strain $\gamma$, are extracted to compare flattened target and 2D precursor. "p31m" BAM unit cells ($\varphi_1 = \varphi_2 = \varphi_3 = 60°$) are selected for isotropic scaling, whereas "cm" ABAM unit cells ($\varphi_1 = \varphi_3 = 45°$, $\varphi_2 = 90°$) are chosen for anisotropic scaling. D) Physical realization of 2D precursor and E–G) its 3D deployment.

the key role of nonuniform scaling for 3D bistable deployment, which could not be obtained otherwise with existing isotropically scalable kirigami. We also note that the 3D target surface here is G0 continuous, and it contains only two unit cell designs. For 3D surfaces with more complex shapes, one potential approach is to improve the design of the unit cells with inverse design strategies and optimization algorithms. These methods have been successfully applied in the field of shape-morphing kirigami.[5,6,10,39,40] Although the ABAM specimens in this work cannot resist gravity because they are fabricated with soft rubber sheets, it is possible to create free-standing 3D surfaces by increasing the stiffness of ABAM. For example, we can fabricate ABAM with stiffer materials, while the stress concentration at the hinges can be reduced by tailoring the geometry of the kirigami constituents, such as the living hinges.[55] Another way is to optimize the unit cell design for high stiffness at the bistable state[10] or incorporate exoskeletons, as shown in our demonstration with interlock hooks.

## 3. Discussion and Conclusion

To conclude, our combined semi-analytical, experimental, and numerical investigations have shown that symmetry breaking of slit pattern induces geometric frustration and anisotropic shape morphing in bistable kirigami and controls the trade-offs between bistability and anisotropy of scaling. While symmetry breaking has been used to generate anisotropic response in other metamaterial architectures,[29,41,44,52] this work unlocks anisotropic morphing in kirigami metamaterials and further unveils how symmetry groups affect geometric frustration and their anisotropic bistable shape shifting. For example, "p31m" BAM with threefold rotational symmetry features frustration-free bistable isotropic expansion, "cm" ABAM with lower symmetry undergoes frustrated anisotropic deployment with reduced bistability, and "p1" ABAM with least symmetry exhibits a moderate response that is frustrated and bounded by "cm" ABAM. The shape-morphing capability of symmetry broken kirigami is demonstrated via a set of in-plane and out-of-plane deployments with various target shapes that cannot be achieved without shear strains, the key indicator of anisotropic deformation. This work has thus established the link between symmetry, frustration, and anisotropic bistable deployment in soft kirigami metamaterials, which can offer a new design route for nonuniform shape morphing.

The symmetry-broken kirigami in this work is entirely made of soft elastic materials to accommodate geometric frustration, which limits the stiffness of the kirigami especially in the deployed state. A potential approach to overcome this limitation is to take a multimaterial design strategy with both soft and rigid components, which, for example, could increase the load-bearing capacity of kirigami metamaterials for engineering applications such as impact energy absorption.[14] Moreover, symmetry-broken kirigami can be made responsive to multiphysical stimuli through the integration of active materials, such as shape memory polymers,[63] hydrogels,[64,65] and dielectric elastomers.[66]

While the concluding demonstrations of our work show how to harness slit symmetry breaking to tailor anisotropic deployment in bistable kirigami, our strategy holds generality and can also be extended to other kirigami patterns[31,67] as well as other types of metamaterials[41,68] and metasurfaces.[69,70] For example, the fourfold symmetry of the square-cut motifs can be reduced by changing the square cuts into rectangular cuts, rhombic cuts, parallelogram cuts, trapezoidal cuts, and even arbitrary quadrilateral cuts. Besides symmetry breaking of slit pattern and geometric design, the asymmetric distribution of multiple materials within a structure, e.g., materials with distinct viscoelasticity[71] and coefficient of thermal expansion,[52,72] could also be exploited to attain uncommon yet highly desired anisotropy in properties and functionality for a diverse range of applications in aerospace, robotics, and other sectors.

## Supporting Information

Supporting Information is available from the Wiley Online Library or from the author.

## Acknowledgements

D.P. acknowledges the financial support of the Canada Research Chairs Program, the Natural Sciences and Engineering Research Council of Canada and MITACS. C.Q. acknowledges support from the Fundamental Research Funds for the Central Universities (Grant No. 2023SCU12096) and the National Natural Science Foundation of China (Grant No. 12302219).

## Conflict of Interest

The authors declare no conflict of interest.

## Data Availability Statement

The data that support the findings of this study are available in the Supporting Information of this article.

## Keywords

anisotropic deployment, geometric frustration, kirigami metamaterials, multistable morphing, symmetry

Received: December 5, 2023
Revised: February 24, 2024
Published online:

[1] Y. Tang, J. Yin, *Extreme Mech. Lett.* **2017**, *12*, 77.
[2] L. Mizzi, E. Salvati, A. Spaggiari, J.-C. Tan, A. M. Korsunsky, *Int. J. Mech. Sci.* **2020**, *167*, 105242.
[3] A. Rafsanjani, D. Pasini, *Extreme Mech. Lett.* **2016**, *9*, 291.
[4] J. N. Grima, L. Mizzi, K. M. Azzopardi, R. Gatt, *Adv. Mater.* **2016**, *28*, 385.
[5] M. Konaković-Luković, J. Panetta, K. Crane, M. Pauly, *ACM Trans. Graph.* **2018**, *37*, 106.
[6] G. P. T. Choi, L. H. Dudte, L. Mahadevan, *Nat. Mater.* **2019**, *18*, 999.
[7] Y. Zhang, Z. Yan, K. Nan, D. Xiao, Y. Liu, H. Luan, H. Fu, X. Wang, Q. Yang, J. Wang, W. Ren, H. Si, F. Liu, L. Yang, H. Li, J. Wang, X. Guo, H. Luo, L. Wang, Y. Huang, J. A. Rogers, *Proc. Natl. Acad. Sci. USA* **2015**, *112*, 11757.
[8] X. Zhang, J. Ma, M. Li, Z. You, X. Wang, Y. Luo, K. Ma, Y. Chen, *Proc. Natl. Acad. Sci. USA* **2022**, *119*, 2117649119.
[9] A. Rafsanjani, L. Jin, B. Deng, K. Bertoldi, *Proc. Natl. Acad. Sci. USA* **2019**, *116*, 8200.
[10] T. Chen, J. Panetta, M. Schnaubelt, M. Pauly, *ACM Trans. Graph.* **2021**, *40*, 39.
[11] J. Tao, H. Khosravi, V. Deshpande, S. Li, *Adv. Sci.* **2023**, *10*, 2204733.
[12] L. Jin, S. Yang, *Adv. Mater.* **2023**, *36*, 2308560.
[13] A. K. Brooks, S. Chakravarty, M. Ali, V. K. Yadavalli, *Adv. Mater.* **2022**, *34*, 2109550.
[14] H. Ye, Q. Liu, J. Cheng, H. Li, B. Jian, R. Wang, Z. Sun, Y. Lu, Q. Ge, *Nat. Commun.* **2023**, *14*, 1607.
[15] Y. Li, F. Pan, X. Lin, K. Yang, Y. Ren, W. Yang, Y. Chen, *Int. J. Mech. Sci.* **2023**, *243*, 108044.
[16] L. H. Dudte, E. Vouga, T. Tachi, L. Mahadevan, *Nat. Mater.* **2016**, *15*, 583.
[17] W. M. van Rees, E. Vouga, L. Mahadevan, *Proc. Natl. Acad. Sci. USA* **2017**, *114*, 11597.
[18] J. Boddapati, S. Mohanty, R. K. Annabattula, *Mech. Mater.* **2020**, *144*, 103350.

[19] C. Wang, D. Zhang, J. Li, Z. You, *Int. J. Solids Struct.* **2022**, *251*, 111752.
[20] C. Wang, J.-l. Li, D.-w. Zhang, *Appl. Math. Model.* **2021**, *89*, 1575.
[21] A. Lamoureux, K. Lee, M. Shlian, S. R. Forrest, M. Shtein, *Nat. Commun.* **2015**, *6*, 8092.
[22] S. Babaee, Y. Shi, S. Abbasalizadeh, S. Tamang, K. Hess, J. E. Collins, K. Ishida, A. Lopes, M. Williams, M. Albaghdadi, A. M. Hayward, G. Traverso, *Nat. Mater.* **2021**, *20*, 1085.
[23] F. Zhang, S. Li, Z. Shen, X. Cheng, Z. Xue, H. Zhang, H. Song, K. Bai, D. Yan, H. Wang, Y. Zhang, Y. Huang, *Proc. Natl. Acad. Sci. USA* **2021**, *118*, 2026414118.
[24] A. Rafsanjani, Y. Zhang, B. Liu, S. M. Rubinstein, K. Bertoldi, *Sci. Rob.* **2018**, *3*, eaar7555.
[25] Q. He, R. Yin, Y. Hua, W. Jiao, C. Mo, H. Shu, J. R. Raney, *Sci. Adv.* **2023**, *9*, eade9247.
[26] Y. Hong, Y. Zhao, J. Berman, Y. Chi, Y. Li, H. Huang, J. Yin, *Nat. Commun.* **2023**, *14*, 4625.
[27] Y. Yang, K. Vella, D. P. Holmes, *Sci. Rob.* **2021**, *6*, eabd6426.
[28] L. Liu, G. P. T. Choi, L. Mahadevan, *Proc. R. Soc. London, Ser. A* **2021**, *477*, 20210161.
[29] Y. Chen, W. Ye, R. Xu, Y. Sun, J. Feng, P. Sareh, *Int. J. Mech. Sci.* **2023**, *249*, 108249.
[30] J. N. Grima, A. Alderson, K. E. Evans, *Phys. Status Solidi B* **2005**, *242*, 561.
[31] J. N. Grima, K. E. Evans, *J. Mater. Sci. Lett.* **2000**, *19*, 1563.
[32] Y. Zheng, I. Niloy, P. Celli, I. Tobasco, P. Plucinsky, *Phys. Rev. Lett.* **2022**, *128*, 208003.
[33] Y. Zheng, I. Niloy, I. Tobasco, P. Celli, P. Plucinsky, *Proc. R. Soc. London, Ser. A* **2023**, *479*, 20220665.
[34] X. Guo, X. Ni, J. Li, H. Zhang, F. Zhang, H. Yu, J. Wu, Y. Bai, H. Lei, Y. Huang, J. A. Rogers, Y. Zhang, *Adv. Mater.* **2021**, *33*, 2004919.
[35] C. Coulais, A. Sabbadini, F. Vink, M. van Hecke, *Nature* **2018**, *561*, 512.
[36] Y. Cho, J.-H. Shin, A. Costa, T. A. Kim, V. Kunin, J. Li, S. Y. Lee, S. Yang, H. N. Han, I.-S. Choi, D. J. Srolovitz, *Proc. Natl. Acad. Sci. USA* **2014**, *111*, 17390.
[37] P. Celli, C. McMahan, B. Ramirez, A. Bauhofer, C. Naify, D. Hofmann, B. Audoly, C. Daraio, *Soft Matter* **2018**, *14*, 9744.
[38] L. Liu, G. P. T. Choi, L. Mahadevan, *Phys. Rev. Res.* **2022**, *4*, 033114.
[39] D. M. Sussman, Y. Cho, T. Castle, X. Gong, E. Jung, S. Yang, R. D. Kamien, *Proc. Natl. Acad. Sci. USA* **2015**, *112*, 7449.
[40] X. Dang, F. Feng, H. Duan, J. Wang, *Phys. Rev. E* **2021**, *104*, 055006.
[41] Y. Mao, Q. He, X. Zhao, *Sci. Adv.* **2020**, *6*, eaaz4169.
[42] W. J. Padilla, *Opt. Express* **2007**, *15*, 1639.
[43] C. M. Bingham, H. Tao, X. Liu, R. D. Averitt, X. Zhang, W. J. Padilla, *Opt. Express* **2008**, *16*, 18565.
[44] Z. Cui, Z. Liang, J. Ju, *Mater. Des.* **2022**, *216*, 110532.
[45] M. Stavric, A. Wiltsche, *Nexus Network J.* **2019**, *21*, 79.
[46] A. P. Ramirez, *Nature* **2003**, *421*, 483.
[47] S. H. Kang, S. Shan, A. Košmrlj, W. L. Noorduin, S. Shian, J. C. Weaver, D. R. Clarke, K. Bertoldi, *Phys. Rev. Lett.* **2014**, *112*, 098701.
[48] G. P. T. Choi, L. H. Dudte, L. Mahadevan, *Phys. Rev. Res.* **2021**, *3*, 043030.
[49] K. Liu, P. P. Pratapa, D. Misseroni, T. Tachi, G. H. Paulino, *Adv. Mater.* **2022**, *34*, 2107998.
[50] J. P. Udani, A. F. Arrieta, *Mater. Des.* **2022**, *221*, 110809.
[51] R. E. Newnham, *Properties of Materials: Anisotropy, Symmetry, Structure*, Oxford University Press, Oxford **2004**.
[52] H. Xu, A. Farag, D. Pasini, *J. Mech. Phys. Solids* **2018**, *117*, 54.
[53] L. Jin, R. Khajehtourian, J. Mueller, A. Rafsanjani, V. Tournat, K. Bertoldi, D. M. Kochmann, *Proc. Natl. Acad. Sci. USA* **2020**, *117*, 2319.
[54] E. W. V. Chaves, *Notes on Continuum Mechanics*, Springer, Dordrecht **2013**.
[55] X. Shang, L. Liu, A. Rafsanjani, D. Pasini, *J. Mater. Res.* **2018**, *33*, 300.
[56] D. Hwang, E. J. Barron, A. B. M. T. Haque, M. D. Bartlett, *Sci. Rob.* **2022**, *7*, eabg2171.
[57] C. S. Ha, R. S. Lakes, M. E. Plesha, *Mater. Des.* **2018**, *141*, 426.
[58] D. M. Correa, C. C. Seepersad, M. R. Haberman, *Integr. Mater. Manuf. Innov.* **2015**, *4*, 165.
[59] D. A. Debeau, C. C. Seepersad, M. R. Haberman, *J. Mater. Res.* **2018**, *33*, 290.
[60] C. El Helou, P. R. Buskohl, C. E. Tabor, R. L. Harne, *Nat. Commun.* **2021**, *12*, 1633.
[61] H. C. Ko, M. P. Stoykovich, J. Song, V. Malyarchuk, W. M. Choi, C.-J. Yu, J. B. Geddes Iii, J. Xiao, S. Wang, Y. Huang, J. A. Rogers, *Nature* **2008**, *454*, 748.
[62] L. Wang, Y. Chang, S. Wu, R. R. Zhao, W. Chen, *Nat. Commun.* **2023**, *14*, 8516.
[63] Y. Tang, Y. Li, Y. Hong, S. Yang, J. Yin, *Proc. Natl. Acad. Sci. USA* **2019**, *116*, 26407.
[64] X. Sun, P. Rao, X. He, C. Yang, W. Hong, *J. Mech. Phys. Solids* **2023**, *175*, 105278.
[65] J. Liu, D. Zhong, T. Yin, Z. Chen, B. Liu, P. Wang, S. Qu, G. Kang, *J. Mech. Phys. Solids* **2022**, *167*, 104973.
[66] T. Li, C. Keplinger, R. Baumgartner, S. Bauer, W. Yang, Z. Suo, *J. Mech. Phys. Solids* **2013**, *61*, 611.
[67] X. Ning, X. Wang, Y. Zhang, X. Yu, D. Choi, N. Zheng, D. S. Kim, Y. Huang, Y. Zhang, J. A. Rogers, *Adv. Mater. Interfaces* **2018**, *5*, 1800284.
[68] L. Lu, S. Leanza, R. R. Zhao, *Appl. Mech. Rev.* **2023**, *75*, 050801.
[69] A.-L. Chen, Y.-S. Wang, Y.-F. Wang, H.-T. Zhou, S.-M. Yuan, *Appl. Mech. Rev.* **2022**, *74*, 020801.
[70] Y. Chen, T. Liu, L. Jin, *Adv. Intell. Syst.* **2022**, *4*, 2100270.
[71] S. Janbaz, K. Narooei, T. van Manen, A. A. Zadpoor, *Sci. Adv.* **2020**, *6*, eaba0616.
[72] M. Xu, Z. Zhao, P. Wang, Y. Zhang, X. Guo, H. Lei, D. Fang, *Acta Mech. Sin.* **2022**, *38*, 421546.